PCCP

ROYAL SOCIETY OF CHEMISTRY

PAPER

View Article Online
View Journal | View Issue

Cite this: *Phys. Chem. Chem. Phys.*, 2024, **26**, 10111

Strain-induced topological phase transition in ferromagnetic Janus monolayer $MnSbBiS_2Te_2$†

Romakanta Bhattarai, Peter Minch, Yunfan Liang, Shengbai Zhang and Trevor David Rhone*

Received 17th November 2023,
Accepted 5th March 2024

DOI: 10.1039/d3cp05578g

rsc.li/pccp

We investigate a strain-induced topological phase transition in the ferromagnetic Janus monolayer $MnSbBiS_2Te_2$ using first-principles calculations. The electronic, magnetic, and topological properties are studied under biaxial strain within the range of −8 to +8%. The ground state of monolayer $MnSbBiS_2Te_2$ is metallic with an out-of-plane magnetic easy axis. A band gap is opened when a compressive strain between −4% and −7% is applied. We observe a topological phase transition at a biaxial strain of −5%, where the material becomes a Chern insulator exhibiting a quantum anomalous hall (QAH) effect. We find that biaxial strain and spin–orbit coupling (SOC) are responsible for the topological phase transition in $MnSbBiS_2Te_2$. In addition, we find that biaxial strain can alter the direction of the magnetic easy axis of $MnSbBiS_2Te_2$. The Curie temperature is calculated using the Heisenberg model and is found to be 24 K. This study could pave the way to the design of topological materials with potential applications in spintronics, quantum computing, and dissipationless electronics.

Introduction

Two-dimensional (2D) magnetic Janus materials are a special class of materials that lack inversion symmetry. Because of their unique crystal structure and strong spin–orbit coupling, they possess many intriguing features, such as Rashba splitting,[1–4] large vertical piezoelectricity,[5–7] a tunable band gap,[8,9] and a large Dzyaloshinskii–Moriya interaction (DMI).[10,11] Therefore, 2D Janus materials have received a great deal of attention in nanoscience and nanotechnology in recent years. To date, several magnetic Janus materials have been discovered experimentally or predicted theoretically. For example, He *et al.* predicted that the Cr-based functionalized Janus MXene monolayers Cr_2CXX' (X, X′ = H, F, Cl, Br, OH) can have a Néel temperature of up to 400 K.[12] Similarly, Akgenc *et al.* predicted a large Curie temperature of 1120 K in the monolayer CrScC, a Cr-based Janus MXene, suggesting a promising candidate for future spintronic applications.[13] Jiao *et al.* proposed new 2D Janus Cr_2O_2XY (X = Cl, Y = Br/I) monolayers and investigated a phase transition from ferromagnetic to antiferromagnetic state with the strain, proposing Cr_2O_2XY as potential materials for the spintronic applications.[14] In addition, Zhang *et al.* predicted a highly stable room-temperature ferromagnetic Janus VSSe monolayer with a large valley polarization, having potential applications in valleytronics $V(S, Se)_2$.[15] The study of these materials with unprecedented properties may provide some useful information for designing functional quantum devices. For example, MoSSe, and WSSe can be used in chemical sensing devices,[16] hydrogen evolution reaction,[17] and photocatalytic water splitting.[18] Similarly, Janus graphene has potential applications in surface functionalization, field-effect transistors, Li-ion batteries, and actuators.[19]

The search for the non-trivial topological features in 2D magnets started in 2019 after experiments identified $MnBi_2Te_4$ (MBT) to be the first antiferromagnetic topological insulator,[20,21] which was already predicted theoretically by Otrokov *et al.* in 2017.[22] Since then MBT has been the major focus of research on 2D materials. In addition, several exotic physical properties of MBT have also been investigated. For example, Lee *et al.* observed that MBT exhibits an intrinsic anomalous Hall effect arising from the noncollinear spin texture in the presence of the magnetic field.[23] Zhang *et al.* predicted the axion insulating phase in the MBT with the quantized magnetocaloric effect.[24] It was later verified by Liu *et al.* in 2020.[25] Deng *et al.* and Liu *et al.* also observed that the Chern insulating phase exists in the few-layer MBT[26,27] Moreover, Li *et al.* predicted several MBT-family materials that have a rich set of magnetic and topological properties such as topological insulators, Chern insulators, and Weyl semimetals[28] In addition, the topological features were also observed in other members of the MBT-family, such as $MnSb_2Te_4$, $MnBi_2Se_4$, and $MnSb_2Se_4$.[29,30] Further to this, several MBT-based heterostructures have also been investigated including $(MnBi_2Te_4)_m(Bi_2Te_3)_n$,[31–33] and MBT/h-BN[34] that exhibit nontrivial topological orders. Materials within the MBT family share

Department of Physics, Applied Physics, and Astronomy, Rensselaer Polytechnic Institute, Troy, NY, 12180, USA. E-mail: rhonet@rpi.edu

† Electronic supplementary information (ESI) available. See DOI: https://doi.org/10.1039/d3cp05578g

the same crystal structure as MBT but with chemical substitutions at the lattice sites.

A monolayer of MBT was first experimentally realized in 2020.[26] Calculations show that MBT is ferromagnetic with an HSE band gap of 0.7 eV.[28] Since MBT is centrosymmetric, it lacks many intriguing physical phenomena, such as piezoelectricity, due to its inversion symmetry. Consequently, many efforts have been made to investigate materials within the MBT family that have small band gaps (required for topological behavior) and large piezoelectric responses. For example, Guo *et al.* theoretically predicted large intrinsic piezoelectricity in the Janus $MnSbBiTe_4$ monolayer.[7] Jiang *et al.* investigated the topological spin-textures in the 2D Janus $MnBi_2(Se, Te)_4$[35] Recently, Wu *et al.* found that the $MnSbBiSe_2Te_2$ Janus monolayer—isostructural to MBT—undergoes a phase transition from a trivial insulator to a topological insulator at −2% strain.[11] Similarly, the Janus $VSiGeN_4$ monolayer was shown to exhibit a trivial semiconductor–metal-QAH insulator transition with the strain.[36] This method of strain engineering has also been applied to bilayers, heterostructures, and bulk materials.[37–42] In addition, an external electric field has also been used to tune the properties of MBT-type materials. Cui *et al.* predicted that the electric control of the topological magnetic phase can be observed in the Janus magnetic $MnBi_2Se_2Te_2/In_2Se_3$ heterostructure.[43] You *et al.* investigated the electric field-induced topological phase transition in the family of monolayer MBT.[44] These materials have potential applications in quantum computing, dissipationless electronics, spintronics,[45] and photoelectric nanodevices.[46]

Recently, a data-driven approach that combines DFT calculations and machine learning was used to predict the properties of several monolayer vdW materials that are isostructural to MBT.[47] The study highlighted several candidate Janus and non-Janus MBT-type materials that could exhibit topological order. While 2D Janus materials have been at the forefront of the current research, there are only a handful of MBT-type Janus materials that have been investigated systematically till now, such as $MnSbBiTe_4$,[7] $MnSbBiSe_2Te_2$[11] and $MnBi_2(S, Se)_2Te_2$.[35] In addition, the behavior of MBT-type materials that exhibit itinerant ferromagnetism in the monolayer hasn't been reported to date. These materials have applications in spintronic devices.[28] This demands a systematic investigation of novel 2D Janus phases in the MBT family that may be useful to provide a deep insight into the behaviors of MBT-type materials. It may also provide avenues for future potential applications in quantum computing, dissipationless electronics, and spintronics. Inspired by this and guided by previous studies, we investigate $MnSbBiS_2Te_2$ a novel Janus ferromagnetic monolayer isostructural to MBT using first-principles calculations. We examine the chemical stability of this phase by calculating the formation energy, the phonon spectra, and *ab initio* molecular dynamics (AIMD) simulations. The calculations show that monolayer $MnSbBiS_2Te_2$ is ferromagnetic with zero band gap and an out-of-plane magnetization direction. The Curie temperature is found to be 24 K, which is comparable to that of other MBT-type materials. We apply a biaxial strain to the $MnSbBiS_2Te_2$ monolayer and investigate changes in the electronic, magnetic, and topological properties within the strain range of −8% to +8%. A band gap appears with a compressive strain between −4% and −7%. We observe a topological phase transition when the biaxial strain reaches −5%. In addition, we find that we can control the magnetic easy axis of $MnSbBiS_2Te_2$ by applying strain. Investigating the impact of strain on monolayer $MnSbBiS_2Te_2$ will help to further explore the electronic, magnetic, and topological degrees of freedom of MBT-type materials.

Methods

We perform density functional theory (DFT) calculations using the VASP package.[48] A projector-augmented-wave (PAW)[49] potential along with the exchange–correlation functional described by the generalized gradient approximation (GGA) of Perdew–Burke–Ernzerhof (PBE) is used for the calculations.[50] To consider the localized states of Mn-3d electrons, we employ a DFT+U method with an effective Hubbard parameter of 4 eV.[51] This value is taken from the literature.[28,46,47,52] A plane wave basis set with an energy cutoff of 500 eV is used for the expansion of the wave function. Spin polarization and the spin–orbit interaction are considered in the calculations. A convergence criterion of 10^{-8} eV is set between any two successive electronic steps. The structures are allowed to relax fully until the force between any two ionic steps is less than 10^{-4} eV Å^{-1}. A gamma-centered k-point mesh of 15 × 15 × 1 is used for the integration of the Brillouin zone. To avoid an interaction between vdW layers caused by the periodic boundary condition, a sufficiently large vacuum space of 45 Å is used along the z-axis. The calculations of topological invariants are performed using the Z2Pack code.[53] The Curie temperature is calculated using Monte Carlo (MC) simulations based on the 2D Heisenberg model implemented in the Mcsolver package.[54] The crystal orbital Hamilton population (COHP) analysis is performed using the LOBSTER package.[55]

Results and discussion

The crystal structure of the $MnSbBiS_2Te_2$ Janus monolayer is shown in Fig. 1. It consists of 7 atoms in a unit cell that are arranged in a septuple layer in the following order: Te–Sb–Te–Mn–S–Bi–S. The Mn atoms are sandwiched between layers of $SbTe_2$ and BiS_2.

This structure is constructed from MBT by replacing Bi with Sb in the upper half and Te with S in the lower half of the MBT

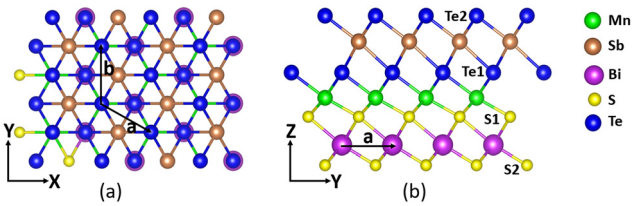

Fig. 1 Crystal structure of monolayer $MnSbBiS_2Te_2$ (a) top view, and (b) side view. The lattice vectors are shown using solid black arrows.

structure. $MnSbBiS_2Te_2$ possesses the same hexagonal lattice as MBT with the optimized lattice constant $a = b = 4.13$ Å, which is $\approx$ 5.7% lower than that of MBT ($a = b = 4.38$ Å). $MnSbBiS_2Te_2$ lacks inversion symmetry because of the asymmetric configurations of the atoms. To find the ground state of monolayer $MnSbBiS_2Te_2$, we consider a $2 \times 1 \times 1$ supercell and perform calculations of ferromagnetic (FM) and antiferromagnetic (AFM) spin configurations. We find that the ground state of $MnSbBiS_2Te_2$ is ferromagnetic with an energy difference of 15.16 meV between FM and AFM states. Calculations show that the magnetic moment of monolayer $MnSbBiS_2Te_2$ is $5\mu_B$ per unit cell.

We also calculate the magnetic anisotropy energy (MAE), which is the difference in energy between the in-plane (100) and out-of-plane (001) spin orientation of magnetic atoms (Mn) as given by the formula:

$$\mathrm{MAE} = E_{||} - E_{\perp} \quad (1)$$

where $E_{||}$ and $E_{\perp}$ are the energies of the in-plane (100) and out-of-plane (001) magnetization directions, respectively. We find that $MnSbBiS_2Te_2$ has an MAE of 287 μeV per Mn atom which is larger than that of MBT (180 μeV).[56] The positive sign indicates that $MnSbBiS_2Te_2$ prefers an out-of-plane magnetization direction. That is, the spin moments of Mn atoms prefer to align along the *z*-axis. See ESI† for details.

We investigate the chemical stability of monolayer $MnSbBiS_2Te_2$ by using three different methods. First, we calculate the formation energy, which is −1.063 eV per unit cell. We use formation energy as a proxy for chemical stability. Next, we perform the phonon dispersion calculations for a more robust check of chemical stability. We use a $4 \times 4 \times 1$ supercell containing 112 atoms using the finite displacement method implemented in the Phonopy package.[57] No imaginary phonon frequencies (that would indicate soft phonon modes) are seen in the phonon dispersion spectrum, thus implying its dynamical stability. The chemical stability is further tested by performing *ab initio* molecular dynamics (AIMD) simulations at 500 K for 30 ps with a time step of 2 fs. The total energy fluctuates without a sudden drop in the energy profile during the entire simulation period. These results provide evidence that monolayer $MnSbBiS_2Te_2$ is chemically stable. See ESI† for details.

To understand the bonding and antibonding states in monolayer $MnSbBiS_2Te_2$, we perform the COHP analysis of monolayer $MnSbBiS_2Te_2$ using the LOBSTER package.[55] The corresponding COHP plots are shown in Fig. 2. The positive (negative) values of −pCOHP represent the bonding (anti-bonding) orbitals. Fig. 1 shows that the valence band mainly consists of bonding orbitals for both spin-up and spin-down components. Also, the anti-bonding orbitals are found mostly near or above the Fermi level that constitutes the conduction band. The strength of interactions can be measured by doing the integral of the COHP (ICOHP). The negative values of ICOHP in all the COHP plots indicate the strong bonding nature among the constituting elements in the monolayer $MnSbBiS_2Te_2$.

To get further deeper into the electronic properties, we perform the Bader charge analysis of the monolayer $MnSbBiS_2Te_2$.[58] We find that the elements occupying the X sites (*i.e.* S and Te) get the electronic charge transferred from the Mn, Sb, and Bi atoms. The Mn atom loses a charge of 1.109*e*, where '*e*' is the charge of an electron, and its value is 1.67×10^{-19} C. This charge is transferred to the Te (0.461*e*) and S (0.648*e*) atoms that are bonded to the Mn atoms (*i.e.* Te1 and S1 respectively). Similarly, the Sb atom loses a charge of 0.594*e*, which is shared between two Te atoms (Te1 in the bulk and Te2 on the surface) as 0.259*e* and 0.335*e* respectively. Similarly, the Bi loses a charge of 1.244*e* and is shared by two S atoms (S1 in the bulk and S2 on the surface) as 0.468*e* and 0.776*e*, respectively. Thus, the Te atom on the surface gets a total charge of 0.335*e*, while that in the bulk gets 0.720*e*. Similarly, the S atom on the surface gets a total charge of 0.776*e*, while that in the bulk gets 1.116*e*. This mechanism implies that the elements occupying the X-sites in the $MnSbBiS_2Te_2$ are more electronegative than those of the A, and B sites.

We plot the total density of states and projected density of states of the monolayer $MnSbBiS_2Te_2$ using the DFT+*U* and hybrid-DFT (*i.e.* HSE06) methods[59,60] by considering the spin–orbit interactions as shown in Fig. 3. We find that the DOS plots from

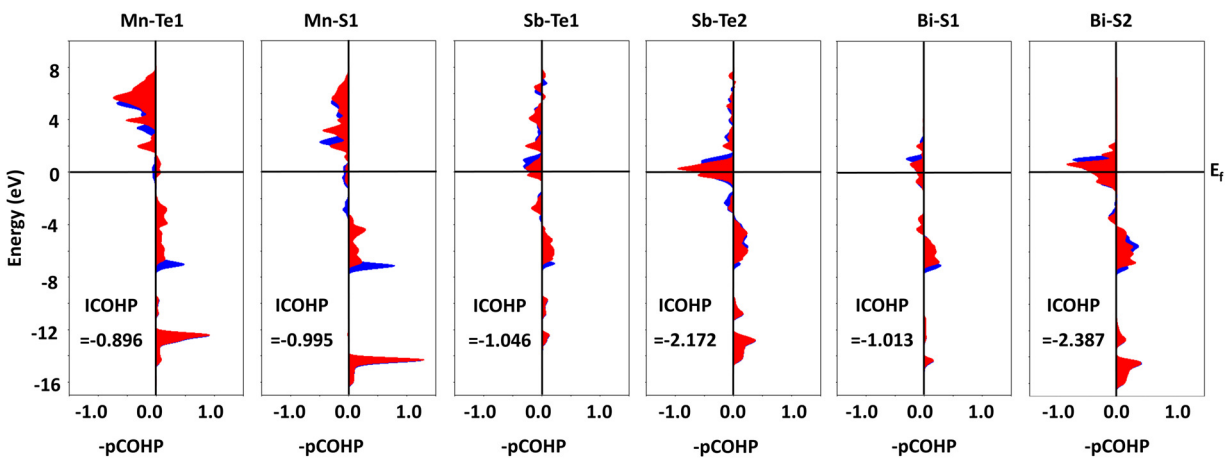

Fig. 2 COHP plots of bonding among the elements that comprise the monolayer $MnSbBiS_2Te_2$. The blue and red colors represent the spin-up and spin-down components, respectively. The corresponding integral COHP (ICOHP) values are also shown. The Fermi level is set to 0 eV.

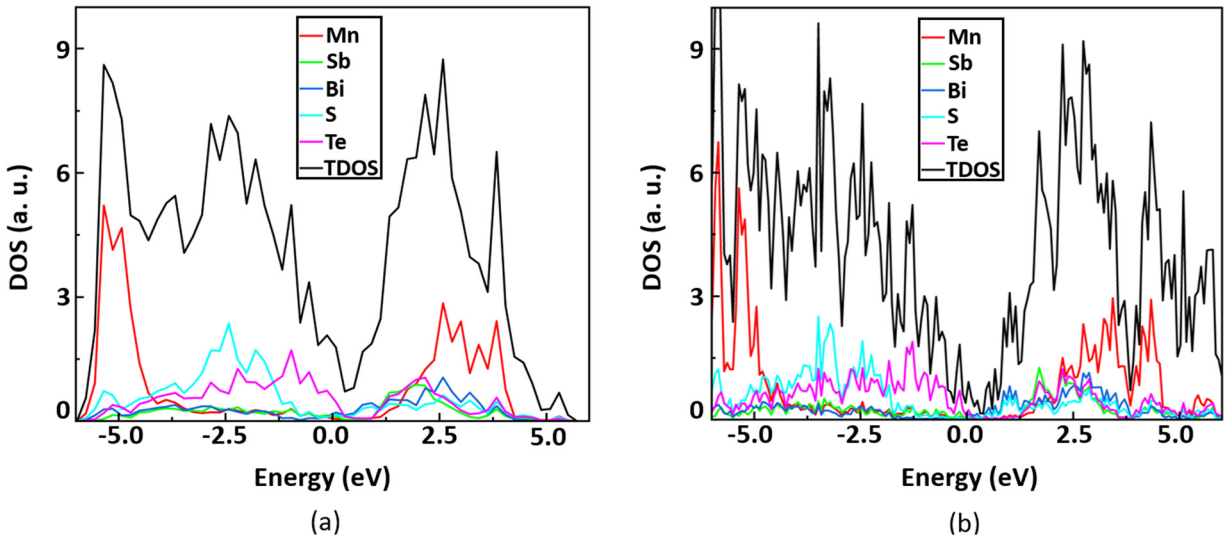

Fig. 3 The total density of states and the projected density of states of the monolayer $MnSbBiS_2Te_2$ using (a) DFT+U, and (b) HSE method. The Fermi level is set to 0 eV.

both methods are similar and confirm the metallic character of the monolayer $MnSbBiS_2Te_2$. This validates the results of the DFT+U method. In Fig. 3(a), we find that Mn has a major contribution to both the valence band (VB) and conduction band (CB) but is far from the Fermi level (E_f). When talking about the contribution near E_f, we find that Bi and S contribute mainly to the CB, while Te contributes to the VB. The contribution of the Sb atom near E_f is very small although its contribution is significant to both the VB and CB far from E_f. A similar behavior is observed in Fig. 3(b). This also resembles the element-decomposed band structure in Fig. 6(a).

In the monolayer $MnSbBiS_2Te_2$, only the elements occupying A sites, namely Mn, are magnetic while all other elements are non-magnetic. However, the non-magnetic atoms still have very small but non-zero local magnetic moments arising from the indirect exchange and super–exchange interactions with the magnetic Mn atoms. Although they have a negligible contribution to the overall magnetic moment, the selection of these elements still affects the magnetic ordering of the material.[47,61] Also, the unpaired spin-up electrons present in extremely localized 3d orbitals in the Mn atom are responsible for this magnetic behavior and the resulting magnetic dipole moment. In the monolayer $MnSbBiS_2Te_2$, Mn atom loses two 4s electrons, so it has a valency of +2. In addition, there is one 3d electron filling up each spin-up Mn-d sub-orbital, and there are 5 such sub-orbitals in Mn. Hence, the total number of spin-up electrons will be 5, and the local magnetic moment of Mn is $5\mu_B$.

Next, we calculate the Curie temperature (T_C) of the $MnSbBiS_2Te_2$ monolayer using Monte Carlo simulations based on the Heisenberg model. The effect of localized 3d-orbitals of Mn atoms is taken into account by considering the following spin Hamiltonian:

$$H = -J\sum_{i,j} S_i \cdot S_j - A\sum_i \left(S_i^z\right)^2 - B\sum_{i,j} S_i^z S_j^z \qquad (2)$$

where J is the isotropic exchange parameter, A is the single-ion anisotropy (SIA), B is the exchange anisotropy, and S_i are the spin vectors for each Mn atom. For a pure MBT monolayer, the value of exchange anisotropy is very small as compared to SIA.[62] So, the effect of B was not considered in the T_C calculations.[44,63] This also holds for the other members of the MBT-type materials such as $MnSbBiTe_4$,[7] $MnSbBiSe_2Te_2$,[11] $MnBi_2S_2Te_2$,[35,64] $MnBi_2Se_2Te_2$,[35,64] and VGa_2Te_4.[65] However, this trend is opposite to the CrI_3-type materials where B is significantly higher as compared to SIA. Since $MnSbBiS_2Te_2$ belongs to a member of MBT-type materials, we don't consider the effect of B in our work, assuming that B has very little influence on T_C.

We consider the first, second, and third nearest neighbor exchange interactions while calculating the magnetic exchange parameters. The calculated values of J_1, J_2, and J_3 are 1.994, −0.092, and −0.035 meV respectively. We find that J_2 and J_3 have very small values as compared to J_1. Also, the negative signs in J_2 and J_3 imply that the second and third nearest neighbors always favor the AFM configurations. However, because of their much weaker strength as compared to J_1, they are dominated by J_1, which always favors the FM coupling. Hence, the preferred configuration of monolayer $MnSbBiS_2Te_2$ is FM. The dominating nature of J_1 favoring FM state is also found in other members of the MBT-type materials such as $MnBi_2Te_4$, $MnSbBiTe_4$, and $MnSbBiSe_2Te_2$ monolayers.[7,11,44] Other methods also exist to model the magnetic structure of the materials using the Heisenberg Hamiltonian.[66]

Since the total magnetic moment of monolayer $MnSbBiS_2Te_2$ is $5\mu_B$ per unit cell, we consider $S = 5/2$ for the Mn atoms. The calculated value of A is 287 μeV per Mn atom. It should be noted that the normalized value of $|S|$ is used when calculating the magnetic exchange parameters. We use the Wolff algorithm along with a supercell of size 50 × 50 × 1 and a temperature range of 1 to 55 K in the MC simulations. A plot of the magnetic moment and the magnetic susceptibility as a function of simulation temperature is shown in Fig. 4(a). The Curie temperature corresponds to the state where the magnetic susceptibility has its peak value. The predicted T_C is found to be 24 K,

which is larger than that of $MnBi_2Te_4$, $MnSbBiTe_4$, $MnSbBiSe_2Te_2$, and $MnBi_2Se_2Te_2$ monolayers.[7,11] It is smaller than that of monolayer $MnBi_2S_2Te_2$.[44]

It is well-known that the Heisenberg model is valid for materials with localized magnetic ordering. However, although monolayer $MnSbBiS_2Te_2$ is a ferromagnetic metal, the local magnetic moment of the Mn atom is very large (*i.e.* $5\mu_B$). This suggests that the Stoner model might be suitable for analyzing the magnetic properties of monolayer $MnSbBiS_2Te_2$. Thus, to justify the applicability of the Heisenberg model, we calculate the Stoner excitation energy ($\langle\varepsilon_k\rangle$)[67] and find it to be 0.92 eV. Since this value is much larger than T_C of $MnSbBiS_2Te_2$ which is 24 K ($\approx$ 2.07 meV), the ratio of the thermal energy of the FM transition (*i.e.* T_C) to $\langle\varepsilon_k\rangle$ is very small. Thus, the effect of Stoner excitation won't be strong near the FM phase transition. So, we expect that the Heisenberg model should work just as a low-energy approximation for $MnSbBiS_2Te_2$. Notably, we expect this approximation to break down as the temperature increases beyond the FM transition and the Stoner excitation becomes relevant to the system. The Heisenberg model has been applied to many other famous 2D ferromagnetic metals including Fe_3GeTe_2[67,68] and $MnSe_2$.[69]

We also calculate the T_C using the analytical formula proposed by Torelli *et al.*[70] and compare it with the result obtained from the MC simulations. Using the analytical formula, we find the T_C to be 34.5 K, which is 10.5 K larger than the T_C obtained from the MC simulations. It is apparent that the closed-form formula overestimates the T_C of monolayer $MnSbBiS_2Te_2$. However, the above analytical formula can be a good source for getting a rough estimate of the T_C for the magnetic materials.

We investigate the electronic, magnetic, and topological properties of monolayer $MnSbBiS_2Te_2$ under biaxial strain. The strain is defined as $\varepsilon = \frac{a - a_0}{a_0}$, where a and a_0 are the lattice constants of strained and unstrained structures respectively. A positive (negative) value of ε indicates a tensile (compressive) strain. We also analyze the effect of biaxial strain on the magnetic easy axis of the monolayer $MnSbBiS_2Te_2$. In the range between −8% and +8% strain, we find that the monolayer $MnSbBiS_2Te_2$ prefers in-plane spin orientation from −3% to −4%. In all other cases, it prefers the out-of-plane spin orientation. See ESI† for details.

The strain dependence on the electronic band gap of monolayer $MnSbBiS_2Te_2$ is also investigated (see Fig. 4(b)). $MnSbBiS_2Te_2$ is metallic at 0% strain, but becomes an insulator when the compressive strain reaches −5%. At −5% strain, a gap is opened near the Γ point with a value of 41.39 meV, which changes to 57.5 meV at −6%, and 21.7 meV at −7% strain. If the strain is increased further, the metallic phase returns. As mentioned above, $MnSbBiS_2Te_2$ prefers an in-plane easy axis with no band gap at −4%. However, we find a small band gap (22.7 meV) when the magnetization axis is artificially switched to the out-of-plane ($M \parallel Z$) direction. The previous reports show that the artificial switching of the magnetization axis in 2D magnets is feasible by applying a large external magnetic field.[71,72] Meanwhile, tensile strain does not open a band gap in monolayer $MnSbBiS_2Te_2$. See ESI† for details.

The band structure of monolayer $MnSbBiS_2Te_2$ at −5% strain is shown in Fig. 5. Fig. 5(a) shows the band structure with the SOC excluded from calculations. In the case of no SOC, the band gap is 0.18 eV. When SOC is turned on, the band gap is reduced to 41.39 meV (see Fig. 5(b)). The elemental-decomposed band structure is calculated and displayed in Fig. 6. The band inversion is not observed where the SOC is turned off. However, we see a clear band inversion near the Fermi level when the SOC is turned on (Fig. 6(b)). Thus the SOC-induced band inversion in strained $MnSbBiS_2Te_2$ indicates a possible topological phase transition. Several studies have shown that SOC plays a vital role in non-trivial

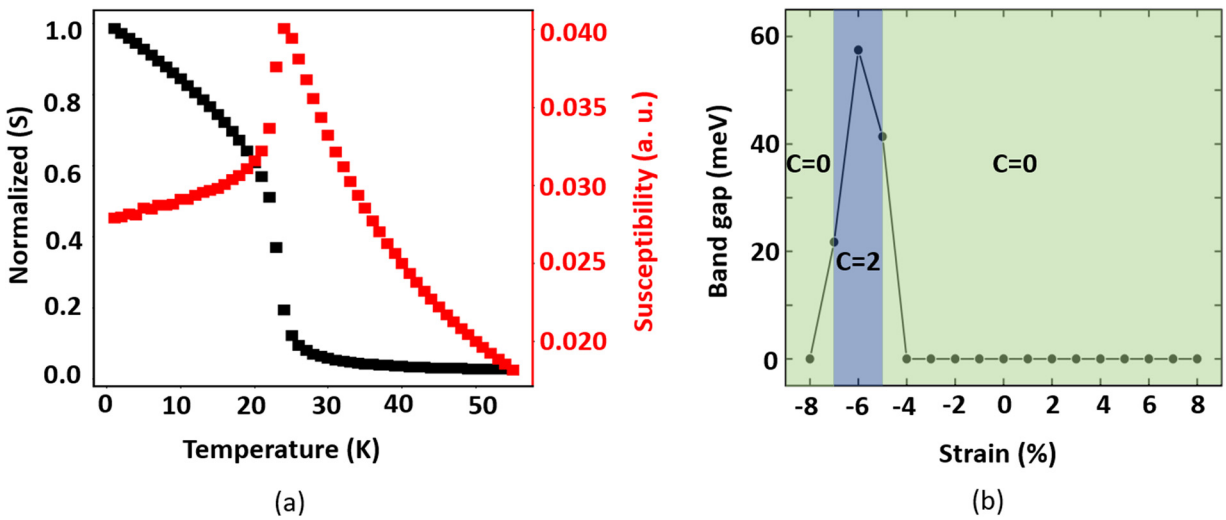

Fig. 4 (a) The normalized spin (S) and magnetic susceptibility of monolayer $MnSbBiS_2Te_2$ as a function of temperature (b) strain-induced topological phase transition in monolayer $MnSbBiS_2Te_2$. The shaded region (light blue color) represents the range of biaxial strain where the monolayer $MnSbBiS_2Te_2$ exhibits Chern insulating phase with C = 2, where C is the Chern number.

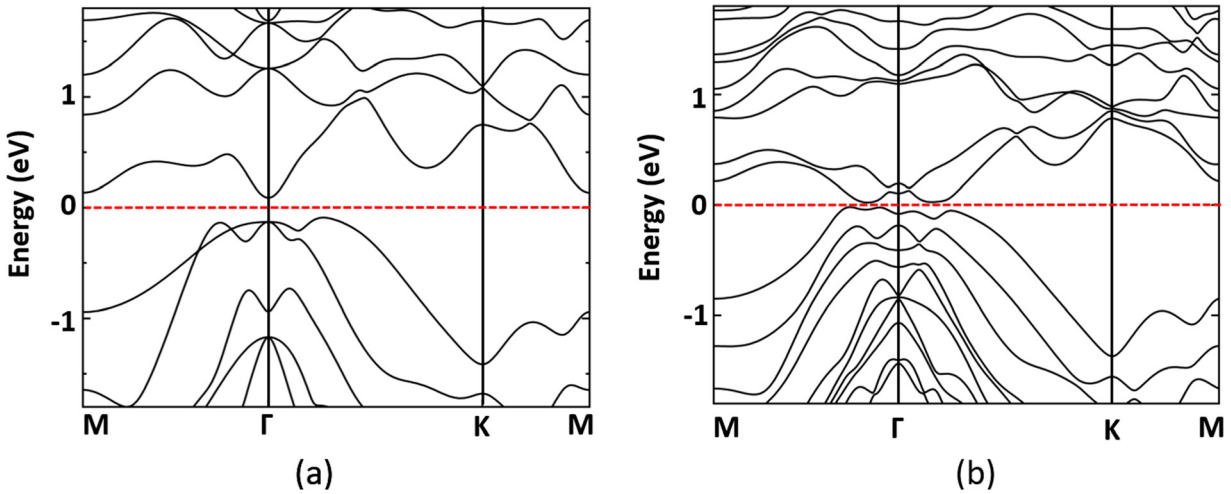

Fig. 5 Electronic band structure of the $MnSbBiS_2Te_2$ Janus monolayer at −5% strain (a) without SOC, and (b) with SOC.

topology because of the fact that SOC-induced band inversion is important for determining the existence of topological phases in the materials.[11,28,44,52,73,74]

The changes in the band gap can be explained by plotting the band structure at different values of strain along the high-symmetry path of the Brillouin zone. The band structure of the unstrained monolayer features a small overlap of the valence band (VB) and conduction band (CB) near the Fermi level. The overlap between VB and CB decreases with increasing compressive strain, then vanishes at −5%; followed by a band gap of 41.39 meV emerging near the Γ point. This gap changes to 57.5 meV at −6% and 21.7 meV at −7% strain. If the compressive strain is further applied, the material changes back to the metallic state. To confirm the metallic phase, we plot the band structure at −8% strain, which shows that the monolayer $MnSbBiS_2Te_2$ is indeed metallic at a biaxial strain of −8%. The band gap is not observed when the strain is applied in the positive direction. See ESI† for details.

To get a deeper insight into the origin of the band gap and the topological phase transition in monolayer $MnSbBiS_2Te_2$, we calculate the charge densities at the highest occupied energy band in the VB and lowest unoccupied energy band in the CB at different values of biaxial strain and follow their changes with the strain (see ESI†). The continuous change of the atomic orbitals with applied strain is observed in Te, Bi, and S atoms for both compressive and tensile strain. Interestingly, no change is observed in the 3d orbitals of Mn atoms throughout the strain range. This behavior is consistent with the elemental-decomposed band structure in Fig. 6. See ESI† for details.

The element-decomposed electronic band structure of unstrained monolayer $MnSbBiS_2Te_2$ is shown in Fig. 6(a). The 5s and 5p orbitals of the Te atoms contribute to the valence bands near the Fermi level while those of the conduction bands are from the joint contributions of the 3p orbitals of S and 6p orbitals of Bi atoms. The band crossings at two different points near the Fermi level indicate the possible topological states in

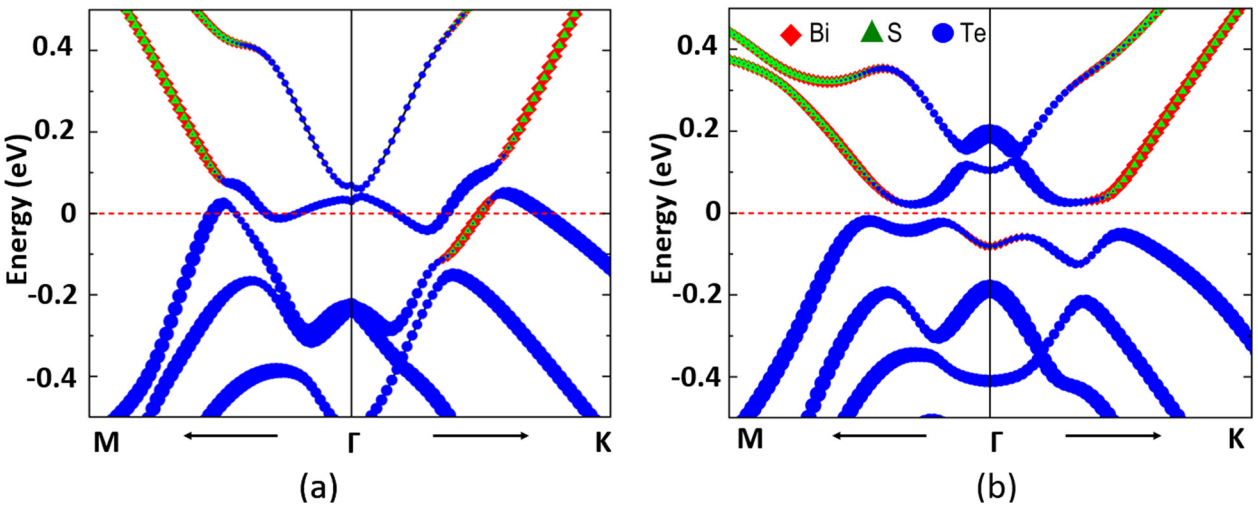

Fig. 6 Element-decomposed band structure of the $MnSbBiS_2Te_2$ Janus monolayer (a) unstrained structure, and (b) at −5% strain. The orbital contributions of Bi, S, and Te atoms are shown in red (diamond), green (triangle), and blue (circle) respectively.

monolayer $MnSbBiS_2Te_2$. When the applied strain reaches −5% (Fig. 6(b)), the overlapping regions on both sides of the Γ point disappear and a clear separation of VB and CB is observed. This results in an indirect band gap of 41.39 meV. We find that the biaxial strain not only changes the lattice parameters and the relative positions of ions in the crystal structure but also contributes to the change of atomic orbitals near the Fermi level. This potentially leads to the opening or closing of the energy gap at different values of strain in addition to SOC-induced band inversion. Hence, strain in the presence of SOC facilitates a topological phase transition.

We observe a band inversion of s and p orbitals of S and Bi atoms (CB → VB), and Te atoms (VB → CB) in the band structure in Fig. 6(b). This indicates a possible topological phase transition in the material at −5% strain (Fig. 4(b)). To confirm this transition, we perform calculations to determine the topological invariant (*i.e.* Chern number) using the Z2Pack package. From the calculations, we find a Chern number (C) = 2, thus confirming a Chern insulator state that exhibits the quantum anomalous hall (QAH) effect. This implies that the Hall conductivity is quantized at $\sigma_{xy} = \frac{2e^2}{h}$. Thus there exist two topologically protected chiral edge states that are capable of carrying a dissipationless current. We find that the QAH insulating phase remains unchanged with C = 2 until the applied strain reaches −8%. At −8% strain, the material goes back to the trivial metallic phase as shown in Fig. 4(b). We also investigate the Chern insulating phases where the magnetization directions are artificially switched between in-plane and out-of-plane. Interestingly, no QAH state is found when the spin magnetization is changed to an in-plane, which is different from the $MnSbBiSe_2Te_2$ monolayer.[11] Our calculations suggest that the trivial insulating phase does not exist in the $MnSbBiS_2Te_2$ monolayer.

Now we investigate the effect of the Hubbard U parameter on the electronic and magnetic properties of monolayer $MnSbBiS_2Te_2$. When dealing with materials that contain strongly correlated electrons, such as transition metals, and rare-earth elements, it is extremely important to make sure that the electron correlations among all the localized d- and f-orbitals are properly addressed in the calculations. Otherwise, there will be convergence issues. *i.e.* the structures may not converge or converge to an incorrect configuration. The DFT+U method solves this issue by adding the Coulomb interaction *via* the Hubbard U parameter; thereby overcoming a main drawback of the standard DFT method. While the DFT+U method is widely used to accurately characterize such materials, it is important to note that it still has its own set of limitations. For example, the choice of the Hubbard U parameter requires careful consideration. Although the value of U is taken from the literature, we validate our results by considering different U values. We perform calculations of electronic and magnetic properties of the monolayer $MnSbBiS_2Te_2$ using the DFT, DFT+U with varying U values (U = 2, 3, 4, 5 eV), and the HSE methods and compare the results. We find that the standard DFT method with zero U value results in monolayer $MnSbBiS_2Te_2$ relaxing to the wrong magnetic configuration (*i.e.* AFM). To further verify this, we repeat the same calculations for the monolayer MBT, which is a well-known ferromagnetic material.[20,28] We find that the MBT also converges to the AFM configuration, which is incorrect. This confirms that the results of the standard DFT alone (*i.e.* without U) are not reliable for predicting the properties of the MBT-type materials. The results of DFT+U (U = 2, 3, 4, 5 eV), and HSE methods are summarized in Table 1.

Where ΔE is the energy difference between AFM and FM configurations (*i.e.* $\Delta E = E_{AFM} - E_{FM}$). Table 1 shows that ΔE is positive and it increases with the Hubbard U parameter showing that $MnSbBiS_2Te_2$ always prefers FM ground state in the considered U range. The larger values of ΔE depict the enhanced magnetic coupling in $MnSbBiS_2Te_2$. Although the MAE decreases with an increase in U value, the easy axis of $MnSbBiS_2Te_2$ always remains the same (*i.e.* OOP) regardless of the U values. As the Hubbard U parameter increases, the strength of J_1 increases while J_2 and J_3 decreases. The nature of FM and AFM exchange couplings remains the same in the considered U range. Thus, by incorporating the U parameter in the calculation, we are able to achieve the correct magnetic configuration of monolayer $MnSbBiS_2Te_2$. In addition, all the methods, including HSE, show the metallic character of monolayer $MnSbBiS_2Te_2$ at 0% strain (unstretched case), whereas at −5% strain, the gap changes with U values almost negligibly. This is because the atomic orbitals of Bi, S, and Te are mainly responsible for determining the band gap of $MnSbBiS_2Te_2$ as shown in the element decomposed band structures in Fig. 6. The d-orbitals of Mn, where the electron correlation effect is applied, are far away from the Fermi level. Hence, they have very little influence in determining the band gap. The band gap at U = 4 eV is close to the result from the HSE calculation, which validates our results.

While it is challenging to experimentally achieve the large compressive strains we predict are required for a phase transition, our results are still useful for understanding the topological properties of MBT-type materials. We expect that our

Table 1 Properties of monolayer $MnSbBiS_2Te_2$ calculated using the DFT+U (U = 2, 3, 4, 5 eV), and HSE methods

Method	ΔE (meV)	MAE (μeV)	Easy axis (IP/OOP)	J_1 (meV)	J_2 (meV)	J_3 (meV)	Band gap at 0% (meV)	Band gap at −5% (meV)
DFT+2 eV	10.118	317	OOP	1.468	−0.188	−0.122	0	61.934
DFT+3 eV	13.442	296	OOP	1.821	−0.130	−0.069	0	50.040
DFT+4 eV	15.156	287	OOP	1.994	−.092	−0.035	0	40.650
DFT+5 eV	15.905	233	OOP	2.056	−0.066	−0.012	0	34.212
HSE	–	–	–	–	–	–	0	46.141

study will create the impetus to search for other magnetic 2D materials that exhibit topological features without applying strain or materials that can undergo topological phase transitions at lower strain. Further to this, our work will also encourage future experimental investigations of these types of materials. It will be interesting to investigate the bilayers, multilayers, and heterostructures of $MnSbBiS_2Te_2$. Materials exhibiting tunable topological features have potential applications in devices with dissipationless transport, topological quantum electronics, and spintronics.

Conclusions

In summary, we propose a novel phase of monolayer $MnSbBiS_2Te_2$ using first-principles calculations. We investigate the chemical stability of $MnSbBiS_2Te_2$ using formation energy calculations, phonon spectra calculations, and AIMD simulations. Calculations show that unstrained monolayer $MnSbBiS_2Te_2$ is ferromagnetic with a zero band gap and an out-of-plane magnetization direction. The calculated Curie temperature is 24 K. We show that applying a biaxial strain to monolayer $MnSbBiS_2Te_2$ alters its electronic, magnetic, and topological properties. A band gap emerges when a compressive strain between -4% and -7% is applied. We also observe a metal-insulator-metal transition with applied strain. The material becomes a Chern insulator with $C = 2$ exhibiting the QAH effect when it is compressed to -5%. Our study provides some important features of the 2D magnetic topological material belonging to the MBT family which may serve as a potential candidate for future applications in topological quantum computing, magnetic sensors, and spintronics. This study also creates new avenues for the strain engineering of topological phase transitions in novel 2D materials with long-range magnetic order.

Author contributions

T. R. conceived the idea of the project and assisted in writing the manuscript. R. B. performed the calculations, conducted the data analysis, and wrote the manuscript. P. M., Y. L., and S. Z. assisted with the data analysis.

Conflicts of interest

There are no conflicts to declare.

Acknowledgements

This work used the Extreme Science and Engineering Discovery Environment (XSEDE), supported by National Science Foundation grant number ACI-1548562. In addition, we used the resources of the Argonne Leadership Computing Facility, which is a DOE Office of Science User Facility supported under Contract DE-AC02-06CH11357. This material is based upon work supported by the NSF CAREER award under grant number 2044842. The authors thank Allan H. MacDonald (University of Texas at Austin), Chao Lei (University of Texas at Austin), and Kin Fai Mak (Cornell University) for useful discussions.

Notes and references

1 Y. Cheng, Z. Zhu, M. Tahir and U. Schwingenschlögl, *Europhys. Lett.*, 2013, **102**, 57001.
2 Y. Wang, W. Wei, H. Wang, N. Mao, F. Li, B. Huang and Y. Dai, *J. Phys. Chem. Lett.*, 2019, **10**, 7426–7432.
3 J. Liang, Q. Cui and H. Yang, *Phys. Rev. B*, 2020, **102**, 220409.
4 Q.-F. Yao, J. Cai, W.-Y. Tong, S.-J. Gong, J.-Q. Wang, X. Wan, C.-G. Duan and J. Chu, *Phys. Rev. B*, 2017, **95**, 165401.
5 L. Dong, J. Lou and V. B. Shenoy, *ACS Nano*, 2017, **11**, 8242–8248.
6 Y. Guo, S. Zhou, Y. Bai and J. Zhao, *Appl. Phys. Lett.*, 2017, **110**, 163102.
7 S.-D. Guo and M.-X. Wang, *Phys. Chem. Chem. Phys.*, 2021, **23**, 22443–22450.
8 W. Chen, X. Hou, X. Shi and H. Pan, *ACS Appl. Mater. Interfaces*, 2018, **10**, 35289–35295.
9 A. Kandemir and H. Sahin, *Phys. Rev. B*, 2018, **97**, 155410.
10 J. Liang, W. Wang, H. Du, A. Hallal, K. Garcia, M. Chshiev, A. Fert and H. Yang, *Phys. Rev. B*, 2020, **101**, 184401.
11 Z. Wu, Y. Xue, Z. Shen and C. Song, *Phys. Chem. Chem. Phys.*, 2023, **25**, 96–105.
12 J. He, P. Lyu, L. Sun, A. M. Garcia and P. Nachtigall, *J. Mater. Chem. C*, 2016, **4**, 6500–6509.
13 B. Akgenç, E. Vatansever and F. Ersan, *Phys. Rev. Mater.*, 2021, **5**, 083403.
14 J. Jiao, N. Miao, Z. Li, Y. Gan, J. Zhou and Z. Sun, *J. Phys. Chem. Lett.*, 2019, **10**, 3922–3928.
15 C. Zhang, Y. Nie, S. Sanvito and A. Du, *Nano Lett.*, 2019, **19**, 1366–1370.
16 C. Jin, X. Tang, X. Tan, S. C. Smith, Y. Dai and L. Kou, *J. Mater. Chem. A*, 2019, **7**, 1099–1106.
17 D. Er, H. Ye, N. C. Frey, H. Kumar, J. Lou and V. B. Shenoy, *Nano Lett.*, 2018, **18**, 3943–3949.
18 L. Ju, M. Bie, X. Tang, J. Shang and L. Kou, *ACS Appl. Mater. Interfaces*, 2020, **12**, 29335–29343.
19 S.-W. Ng, N. Noor and Z. Zheng, *NPG Asia Mater.*, 2018, **10**, 217–237.
20 M. M. Otrokov, I. I. Klimovskikh, H. Bentmann, D. Estyunin, A. Zeugner, Z. S. Aliev, S. Gaß, A. Wolter, A. Koroleva and A. M. Shikin, *et al.*, *Nature*, 2019, **576**, 416–422.
21 Y. Gong, J. Guo, J. Li, K. Zhu, M. Liao, X. Liu, Q. Zhang, L. Gu, L. Tang and X. Feng, *et al.*, *Chin. Phys. Lett.*, 2019, **36**, 076801.
22 M. M. Otrokov, T. V. Menshchikova, M. G. Vergniory, I. P. Rusinov, A. Y. Vyazovskaya, Y. M. Koroteev, G. Bihlmayer, A. Ernst, P. M. Echenique and A. Arnau, *et al.*, *2D Mater.*, 2017, **4**, 025082.
23 S. H. Lee, Y. Zhu, Y. Wang, L. Miao, T. Pillsbury, H. Yi, S. Kempinger, J. Hu, C. A. Heikes and P. Quarterman, *et al.*, *Phys. Rev. Res.*, 2019, **1**, 012011.
24 D. Zhang, M. Shi, T. Zhu, D. Xing, H. Zhang and J. Wang, *Phys. Rev. Lett.*, 2019, **122**, 206401.

25 C. Liu, Y. Wang, H. Li, Y. Wu, Y. Li, J. Li, K. He, Y. Xu, J. Zhang and Y. Wang, *Nat. Mater.*, 2020, **19**, 522–527.
26 Y. Deng, Y. Yu, M. Z. Shi, Z. Guo, Z. Xu, J. Wang, X. H. Chen and Y. Zhang, *Science*, 2020, **367**, 895–900.
27 C. Liu, Y. Wang, M. Yang, J. Mao, H. Li, Y. Li, J. Li, H. Zhu, J. Wang and L. Li, *et al.*, *Nat. Commun.*, 2021, **12**, 4647.
28 J. Li, Y. Li, S. Du, Z. Wang, B.-L. Gu, S.-C. Zhang, K. He, W. Duan and Y. Xu, *Sci. Adv.*, 2019, **5**, eaaw5685.
29 T. Murakami, Y. Nambu, T. Koretsune, G. Xiangyu, T. Yamamoto, C. M. Brown and H. Kageyama, *Phys. Rev. B*, 2019, **100**, 195103.
30 H. Zhang, W. Yang, Y. Wang and X. Xu, *Phys. Rev. B*, 2021, **103**, 094433.
31 E. D. Rienks, S. Wimmer, J. Sánchez-Barriga, O. Caha, P. S. Mandal, J. Růžička, A. Ney, H. Steiner, V. V. Volobuev and H. Groiß, *et al.*, *Nature*, 2019, **576**, 423–428.
32 J. Wu, F. Liu, M. Sasase, K. Ienaga, Y. Obata, R. Yukawa, K. Horiba, H. Kumigashira, S. Okuma and T. Inoshita, *et al.*, *Sci. Adv.*, 2019, **5**, eaax9989.
33 I. I. Klimovskikh, M. M. Otrokov, D. Estyunin, S. V. Eremeev, S. O. Filnov, A. Koroleva, E. Shevchenko, V. Voroshnin, A. G. Rybkin and I. P. Rusinov, *et al.*, *npj Quantum Mater.*, 2020, **5**, 54.
34 R. Gao, G. Qin, S. Qi, Z. Qiao and W. Ren, *Phys. Rev. Mater.*, 2021, **5**, 114201.
35 J. Jiang, X. Liu, R. Li and W. Mi, *Appl. Phys. Lett.*, 2021, **119**, 072401.
36 S.-D. Guo, W.-Q. Mu, J.-H. Wang, Y.-X. Yang, B. Wang and Y.-S. Ang, *Phys. Rev. B*, 2022, **106**, 064416.
37 Z. Tajkov, D. Visontai, L. Oroszlány and J. Koltai, *Nanoscale*, 2019, **11**, 12704–12711.
38 M. Trama, V. Cataudella and C. A. Perroni, *Phys. Rev. Res.*, 2021, **3**, 043038.
39 G. Luo, X. Lv, L. Wen, Z. Li and Z. Dai, *Front. Phys.*, 2022, **17**, 23502.
40 R. Juneja, R. Shinde and A. K. Singh, *J. Phys. Chem. Lett.*, 2018, **9**, 2202–2207.
41 T. Ideue, M. Hirayama, H. Taiko, T. Takahashi, M. Murase, T. Miyake, S. Murakami, T. Sasagawa and Y. Iwasa, *Proc. Natl. Acad. Sci. U. S. A.*, 2019, **116**, 25530–25534.
42 J. Mutch, W.-C. Chen, P. Went, T. Qian, I. Z. Wilson, A. Andreev, C.-C. Chen and J.-H. Chu, *Sci. Adv.*, 2019, **5**, eaav9771.
43 Q. Cui, Y. Zhu, J. Jiang, J. Liang, D. Yu, P. Cui and H. Yang, *Phys. Rev. Res.*, 2021, **3**, 043011.
44 J.-Y. You, X.-J. Dong, B. Gu and G. Su, *Phys. Rev. B*, 2021, **103**, 104403.
45 X.-L. Qi and S.-C. Zhang, *Rev. Mod. Phys.*, 2011, **83**, 1057–1110.
46 Y. An, K. Wang, S. Gong, Y. Hou, C. Ma, M. Zhu, C. Zhao, T. Wang, S. Ma and H. Wang, *et al.*, *npj Comput. Mater.*, 2021, **7**, 45.
47 R. Bhattarai, P. Minch and T. D. Rhone, *J. Mater. Chem. C*, 2023, **11**(17), 5601–5610.
48 G. Kresse and J. Furthmüller, *Phys. Rev. B: Condens. Matter Mater. Phys.*, 1996, **54**, 11169.
49 P. E. Blöchl, *Phys. Rev. B: Condens. Matter Mater. Phys.*, 1994, **50**, 17953.
50 J. P. Perdew, K. Burke and M. Ernzerhof, *Phys. Rev. Lett.*, 1996, **77**, 3865.
51 S. L. Dudarev, G. A. Botton, S. Y. Savrasov, C. Humphreys and A. P. Sutton, *Phys. Rev. B: Condens. Matter Mater. Phys.*, 1998, **57**, 1505.
52 Z. Li, J. Li, K. He, X. Wan, W. Duan and Y. Xu, *Phys. Rev. B*, 2020, **102**, 081107.
53 D. Gresch, G. Autes, O. V. Yazyev, M. Troyer, D. Vanderbilt, B. A. Bernevig and A. A. Soluyanov, *Phys. Rev. B*, 2017, **95**, 075146.
54 L. Liu, X. Ren, J. Xie, B. Cheng, W. Liu, T. An, H. Qin and J. Hu, *Appl. Surf. Sci.*, 2019, **480**, 300–307.
55 S. Maintz, V. L. Deringer, A. L. Tchougréeff and R. Dronskowski, *LOBSTER: A tool to extract chemical bonding from plane-wave based DFT*, 2016.
56 F. Xue, Z. Wang, Y. Hou, L. Gu and R. Wu, *Phys. Rev. B*, 2020, **101**, 184426.
57 A. Togo and I. Tanaka, *Scr. Mater.*, 2015, **108**, 1–5.
58 G. Henkelman, A. Arnaldsson and H. Jónsson, *Comput. Mater. Sci.*, 2006, **36**, 354–360.
59 J. Heyd, G. E. Scuseria and M. Ernzerhof, *J. Chem. Phys.*, 2003, **118**, 8207–8215.
60 J. Heyd and G. E. Scuseria, *J. Chem. Phys.*, 2004, **121**, 1187–1192.
61 T. D. Rhone, W. Chen, S. Desai, S. B. Torrisi, D. T. Larson, A. Yacoby and E. Kaxiras, *Sci. Rep.*, 2020, **10**, 15795.
62 M. N. Gjerding, A. Taghizadeh, A. Rasmussen, S. Ali, F. Bertoldo, T. Deilmann, N. R. Knøsgaard, M. Kruse, A. H. Larsen and S. Manti, *et al.*, *2D Mater.*, 2021, **8**, 044002.
63 Y. Li, Z. Jiang, J. Li, S. Xu and W. Duan, *Phys. Rev. B*, 2019, **100**, 134438.
64 Q. Cui, Y. Zhu, J. Liang, P. Cui and H. Yang, *Phys. Rev. B*, 2023, **107**, 064422.
65 B.-C. Gong, Y. Gao, X.-L. Qiu, N.-N. Zhao, K. Liu and Z.-Y. Lu, *Phys. Rev. B*, 2022, **106**, 235153.
66 S. Tiwari, M. L. Van de Put, B. Soree and W. G. Vandenberghe, *Phys. Rev. B*, 2021, **103**, 014432.
67 Z.-X. Shen, X. Bo, K. Cao, X. Wan and L. He, *Phys. Rev. B*, 2021, **103**, 085102.
68 H. L. Zhuang, P. Kent and R. G. Hennig, *Phys. Rev. B*, 2016, **93**, 134407.
69 J.-J. Liao, Y.-Z. Nie, X.-G. Wang, Z.-Y. Luo, Q.-L. Xia, R. Xiong and G.-H. Guo, *Phys. B*, 2024, **675**, 415642.
70 D. Torelli and T. Olsen, *2D Mater.*, 2018, **6**, 015028.
71 J. Li, C. Wang, Z. Zhang, B.-L. Gu, W. Duan and Y. Xu, *Phys. Rev. B*, 2019, **100**, 121103.
72 Y. Deng, Y. Yu, Y. Song, J. Zhang, N. Z. Wang, Z. Sun, Y. Yi, Y. Z. Wu, S. Wu and J. Zhu, *et al.*, *Nature*, 2018, **563**, 94–99.
73 P. Li, J. Yu, Y. Wang and W. Luo, *Phys. Rev. B*, 2021, **103**, 155118.
74 C. Lin, M. Ochi, R. Noguchi, K. Kuroda, M. Sakoda, A. Nomura, M. Tsubota, P. Zhang, C. Bareille, K. Kurokawa, Y. Arai, K. Kawaguchi, H. Tanaka, K. Yaji, A. Harasawa, M. Hashimoto, D. Lu, S. Shin, R. Arita, S. Tanda and T. Kondo, *Nat. Mater.*, 2021, **20**, 1093–1099.